ADAPTION OF CLASSICAL GRAIN NUCLEATION MODELS FOR THE APPLICATION IN PBF-LB/M MICROSTRUCTURE SIMULATIONS

HANNES PANZER[1], WEIYU ZHAO[1], OEZGUER BOECKUEN[1], DOMINIK RAUNER[1], LUCA REICHERT[2], AND MICHAEL F. ZAEH[1]

[1] Technical University of Munich, TUM School of Engineering and Design, Institute for Machine Tools and Industrial Management (*iwb*)
Boltzmannstr. 15, 85748 Garching, Germany
e-mail: hannes.panzer@iwb.tum.de, wy.zhao@tum.de, oezgur.boeckuen@tum.de, dominik.rauner@iwb.tum.de, michael.zaeh@iwb.tum.de

[2] Technical University of Munich, TUM School of Engineering and Design, Chair of Materials Science
Boltzmannstr. 15, 85748 Garching, Germany
e-mail: luca.reichert@tum.de

Key words: Nucleation modeling, microstructure tailoring, process parameter variation, moving heat source simulation, multi-scale approach, finite element method, laser powder bed fusion, selective laser melting, L-PBF

Summary. In the powder bed fusion of metals using a laser beam (PBF-LB/M), an industrially highly relevant additive manufacturing technology, process parameters, such as the laser power, can be modified locally. This allows for a tailoring of the mechanical properties or a modification of the cracking susceptibility of the manufactured parts. That can be reasoned by the resulting microstructure, which in turn is strongly dependent on grain-initiating nucleation phenomena. Modeling the latter by means of numerical process simulations is, therefore, of high importance to widen the application area of PBF-LB/M. However, currently available nucleation models are either not able to represent the nucleation rates in PBF-LB/M or the models need to be calibrated for each process parameter set, which impedes a first-time-right additive manufacturing. The goal of this study was to adapt a classical nucleation model, which has proven to be a promising approach for PBF-LB/M microstructure simulations, to allow for a prediction of nucleation locations with varying process parameters and geometrical features. For this, various Inconel 718 specimens, expected to exhibit a geometry-related heat accumulation, were experimentally manufactured using different laser powers. The temperature behavior and the grain density were analyzed afterwards. The identical geometries were simulated by means of a finite element multi-scale simulation approach. A macro-scale simulation accounted for the geometrical features and provided the thermal boundaries to the meso-scale moving heat source simulation. The determined thermal values served as an input to the micro-scale simulation, represented by the adapted grain nucleation model. It was shown that the local and the global nucleation predictions agreed well with the experiments. Also, it was observed that the thermal gradient and the solidification rate need to be considered when modeling nucleation phenomena. These investigations contribute to a first-time-right manufacturing considering tailored

microstructures and failure behavior in PBF-LB/M.

1 INTRODUCTION

The manufacturing of geometrically complex parts can be challenging or even impossible with conventional manufacturing technologies, such as milling or casting [1]. Additive manufacturing technologies and, in particular, the powder bed fusion of metals using a laser beam (PBF-LB/M) reduce these manufacturability restrictions. PBF-LB/M additionally allows for local process parameter adaptions to modify the mechanical properties and the failure behavior due to microstructural changes [2]. The grain structure is determined by the preceding grain nucleation. Predicting the nucleation rate at changing process parameters and geometrical features, however, still poses a challenge in numerical simulations.

Koepf et al. [3] determined the microstructure during the powder bed fusion of metals using an electron beam by means of a cellular automaton (CA) approach for the nickel-based superalloy CMSX-4. In their studies, they did not consider nucleation phenomena in the microstructure simulations, by which the predicted grain sizes were larger than the experimental observations.

Xie et al. [4] performed CA simulations of the PBF-LB/M process for the nickel-based superalloy Inconel 625. In their nucleation modeling approach, they integrated a thermal gradient dependency for the crystallographic orientation of the nuclei. The effect of the thermal gradient on the actual nucleation formation was not considered.

Dezfoli et al. [5] established a CA model coupled with the finite element method (FEM) for the titanium alloy Ti-6Al-4V. They determined the total nucleation density depending on the thermal undercooling, which was composed of the current temperature in the melt pool and the melting temperature. As input values to the phenomenological nucleation model, the authors applied calibration constants from the literature. Hence, a first-time-right prediction of the resulting microstructure was not possible.

Regarding the specific analysis of nucleation models, Li and Tan [6] analyzed the effects of nucleation phenomena on the grain structure in metal additive manufacturing by means of a 3D CA model and a phenomenological nucleation model. They observed that the resulting grain structure changed significantly by changing the values for the nucleation model input parameters. The authors stated that the investigation of further nucleation mechanisms for a reliable prediction of the grain formation is needed.

Panzer et al. [7] evaluated physics-based and phenomenological nucleation models in terms of their predictive capabilities for the aluminum alloys Scalmalloy and Scancromal. They identified the heterogeneous nucleation model as the most promising approach when striving for a first-time-right predictability of nucleation locations. However, the applicability of the model to the nickel-based superalloy Inconel 718 (IN718) was not evaluated. No process parameter changes and geometry variations were applied.

Mohebbi and Ploshikhin [8] proposed a nucleation simulation approach for the identification of nucleation locations in the aluminum alloy AlSi10Mg. The model enables a flexible calibration for different materials and process parameters for an application in CA grain simulations. However, a first-time-right manufacturing is not possible with this approach. Also, the transferability to non-aluminum alloys was not discussed.

When considering the modeling of grain formation processes in microstructure simulations for PBF-LB/M, so far, either no nucleation has been considered or phenomenological nucleation approaches requiring an experimental calibration have been utilized. For the undercooling, as the central input parameter to nucleation models, only the melting and local temperature were considered, while temporal and spatial temperature changes were neglected. The effect of process parameter changes and geometrically induced heat accumulation phenomena on the nucleation behavior were not considered in the evaluated studies.

Therefore, the goal of this study was to establish a stand-alone nucleation model to quantify grain density changes and the microstructure homogeneity as a function of process parameters and geometrical features. For this purpose, the research questions to be answered in the course of this paper can be stated as follows:

- How can the global and local thermal behavior be modeled and numerically predicted?

- How are physics-based nucleation models to be extended to consider these thermal phenomena?

- To what extent is a local and global prediction of the grain density, homogeneity, and morphology by a stand-alone nucleation model possible?

2 MATERIALS AND METHODS

In the following, an overview of the utilized geometries and process parameters is given, followed by descriptions of the simulative and experimental setups.

2.1 General specifications

In the course of this study, two geometries were designed to investigate the influence of geometrically induced heat accumulations for IN718. Three process parameter sets were applied to each geometry to additionally analyze the impact of process parameter changes on the resulting microstructure and on the predictive capabilities of nucleation models.

2.1.1 Geometries

The rotationally symmetric specimens are visualized in Figure 1, which are termed specimen 1 (see Figure 1a) and specimen 2 (see Figure 1b). Both samples were placed on a base with a height of 5 mm. The actual parts were characterized by a cylindrical region with a diameter of 3 mm. While for specimen 1, the geometrical shape was not changed any further over the build height, the cross-sectional area of specimen 2 was increased gradually after a height of 10 mm with an overhang angle of 45°. The latter sample was intended to induce a geometrical overheating, while the first sample served as a reference.

2.1.2 Process parameters

As determined by Panzer et al. [2], laser power changes have the highest influence on the microstructure compared to the laser beam scan speed and the hatch distance variations. Therefore, only the laser power was varied in this study and was set to 219 W, 285 W, and 407 W [2], respectively. The scan speed was chosen to be 960 mm/s, the hatch distance was 0.11 mm, and
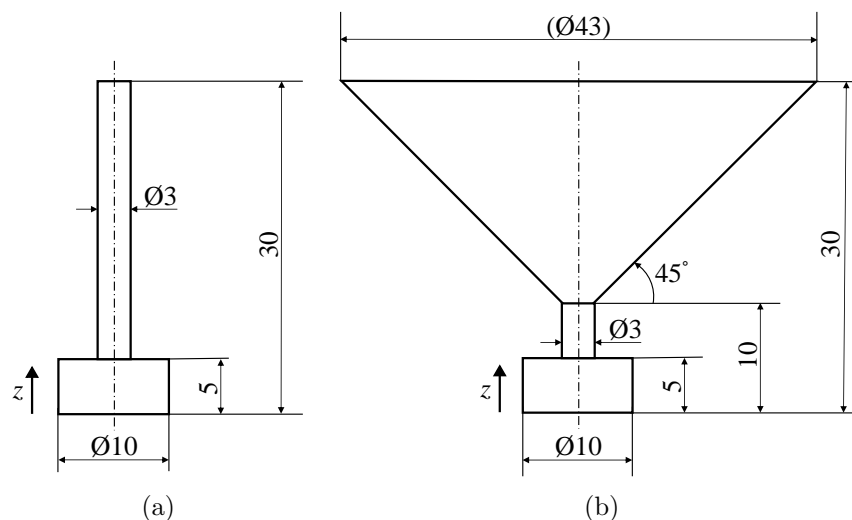
Figure 1: Geometries utilized in this study with dimensions in mm and the building direction z; (a) specimen 1, (b) specimen 2

the layer height was set to 40 μm. The individual parameters were applied to each geometry shown in Figure 1.

2.2 Experimental setup

In the following, the experimental building process, along with the subsequent evaluation procedure during and after the part manufacturing, is explained.

2.2.1 Processing

Each geometry was manufactured three times in a single build job on a PBF-LB/M machine (M400-1, EOS GmbH, Germany) using a silicon recoater for a high process stability. Additionally, two identical blocks with the size of $20 \times 15 \times 10\,\text{mm}^3$ each were manufactured with the medium laser power of 285 W. To the last layer of each block, two single weld lines with each of the three laser powers were applied. These lines were used for a subsequent heat source calibration and a validation of the simulations (see Subsection 2.3.2). No heat treatment was applied to the samples.

The build job was monitored by an optical tomography (OT) system (EOSTATE Exposure OT, EOS GmbH, Germany). This allowed for an observation of the change in the gray values, which can be used to derive the temperature distribution in the parts depending on the laser power and the geometry.

The chemical composition of the powder utilized in the course of this study (MetcoAdd 718C, OC Oerlikon Corporation AG, Switzerland) is listed in Table 1.

2.2.2 Evaluation

Below, the evaluation procedure for investigating both the thermal behavior within the parts as well as for analyzing the resulting grain structure is described.

Table 1: Chemical composition of the utilized IN718 powder material [9]

Element	Ni	Fe	Cr	Nb + Ta	Mo	Al	Ti	C	Other
Share in m.%	Balance	18.00	18.00	5.00	3.00	0.60	1.00	< 0.08	< 0.50

Thermal analysis

The integral gray values of the OT, normalized by the cross-sectional area of each part in the respective layer, were analyzed to evaluate geometrically induced heat accumulations and the thermal influence of the laser power variations.

After the separation of the parts from the build plate, the surfaces of the specimens 1 and 2 were analyzed regarding their annealing colors. Based on the latter, geometrically induced over-heating regions can be detected, their distinctness changing based on the used laser power.

Afterwards, the samples were cut along the building direction in the center of the respective specimen and embedded in epoxy resin. The embedded specimens were ground using SiC abrasive paper, polished with a $3\,\mu m$ diamond suspension, and etched by an etching agent consisting of $40\,ml\ H_2O$, $60\,ml\ HCl$, and $10\,ml\ H_2O_2$.

The block structures were evaluated in terms of the melt pool width and depth of the single weld lines on top with reference to the substrate surface, as illustrated in Figure 2.
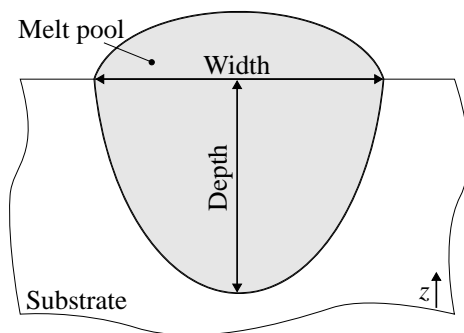

Figure 2: Schematic illustration of the melt pool width and depth measurements for the subsequent simulative heat source calibration and validation; z: building direction

Microstructure analysis

For the specimens 1 and 2, the grain structures considering the grain densities were evaluated for the various laser powers and along the building direction at the global locations 1 to 3 in the center of the specimens as shown in Figure 3. A digital microscope (VHX 7000, Keyence Corp., USA) was used to extract the images with a magnification of $500\times$ of the etched samples. Therefore, each picture had a size of $0.4 \times 0.6\,mm^2$. At each global measurement location, three pictures were taken along the horizontal direction, their centers being equally distributed around the center line with a distance of 0.5 mm each. This allowed to consider statistical deviations in the microstructure and of the measuring method itself. The latter was performed by using an image processing program (*ImageJ*, National Institutes of Health, USA) [10] and its *Analyze Particles* package. Further information about the grain structure characterization can be found in Panzer et al. [2].

The determined grain values were compared to the simulatively predicted nucleation locations (see Subsection 2.3.5). For this, it was assumed that the grain and nucleation density and their
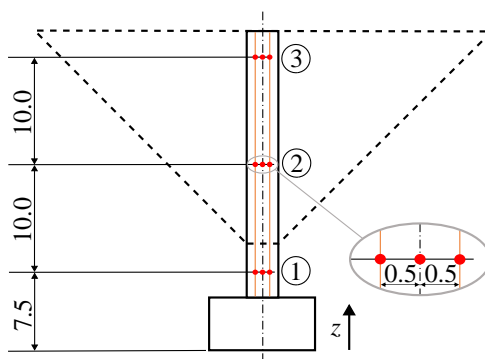
Figure 3: Measurement locations of the microstructure along the build height (specimen 1: continuous line, specimen 2: dashed line) with dimensions in mm and the building direction z

relative changes are directly related to each other. This appeared to be a valid assumption as for each formed grain during the manufacturing process a stable nucleus is a prerequisite.

2.3 Simulation setup

Below, the simulative methods concerning the thermal and the nucleation modeling are described. Also, the material and numerical parameters, along with the subsequent evaluation procedure, are explained.

2.3.1 Overview

To be able to consider the geometrically induced overheating and the thermal behavior due to the process parameter changes, a multi-scale simulation approach was set up.

After a finite element meshing of the whole parts, the global temperatures in the parts were identified based on a macroscopic thermal part scale simulation applying a flash exposure strategy. The temperatures were then utilized as boundary conditions for the subsequent mesoscopic simulations. For the latter, cuboids were extracted from the global sample geometries at certain locations in the center and were remeshed with a decreased element size. Afterwards, a moving heat source simulation was conducted. Within the sub-models, the nucleation evaluations were performed, for which a sub-mesh with a further decreased cell size was established. A visualization of the described process is exemplarily shown for the specimen 2 in Figure 4.

The simulations were executed on a workstation utilizing six logical central processing unit cores of the type AMD EPYC$^{\text{TM}}$ 7343 at a frequency of 3.2 GHz and 64 GB random-access memory.

2.3.2 Heat source setup

Both heat source types, the macroscopic and the mesoscopic, were calibrated to allow for temperature predictions considering geometry and process parameter changes.

Global heat source

The two specimen geometries were thermally simulated by means of a part-scale simulation approach [11, 12] based on the open-source FEM tool CalculiX CrunchiX [13]. There, real layer heights are combined to larger-layer compounds and are applied by the element birth and
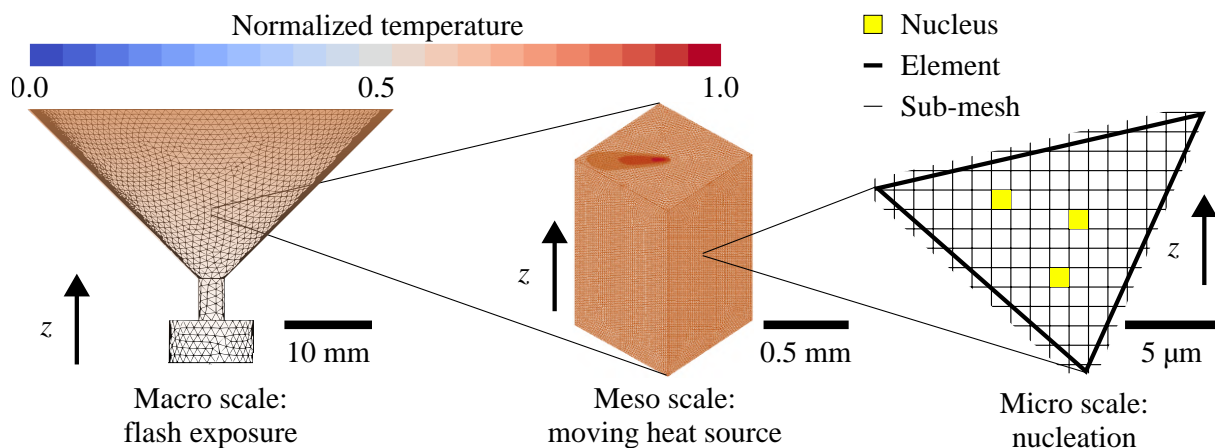
Figure 4: Multi-scale simulation approach for the determination of global nucleation locations with the building direction z

death method [14]. For a further decrease in the computational effort, the laser heat input is simplified by a flash exposure, not taking into account the laser beam scan paths. Each part was individually simulated while being placed on the center of a build plate with side lengths of 250 mm and a thickness of 40 mm.

The parts, along with the build platform, were meshed using an FEM meshing tool (Hypermesh 2023, Altair Engineering, USA). The element size of the build plate was chosen to be 10.0 mm and was decreased in the vicinity of the parts. The temperature-dependent material properties of the plate were set to be those of steel 1.1730, while those of the parts were from IN718 bulk material, which was in accordance with the experiments. The material properties will be further explained in Subsection 2.3.4. For the specimen 2, a mesh convergence study was conducted with the element sizes of 0.5 mm, 1.0 mm, and 2.0 mm. The corresponding layer compound heights were set to be 1.0 mm, 2.0 mm, and 4.0 mm, respectively. These were, therefore, always twice the element size to have a sufficient number of nodes within a layer compound. After the second of ten cooling steps of a standard simulation, the temperature data were evaluated in the center of the sample along the z-axis at three different positions. The latter had a distance of 8 mm from each other.

Afterwards, the cooling time after each exposure step had to be calibrated once to accurately determine the geometrically induced heat accumulations during the building process. For this, the time for the cool down at the medium process parameters was calibrated for the specimen 1, as it maintained a constant cross-section over the complete build height, suggesting that there is no strong temperature increase along the z-axis. The cooling time was, therefore, set to a small value of 1 s and was successively increased to a value, at which only a low heat accumulation towards the process temperature [11] was present. The identified time value was then applied to the specimen 2. To also take into account the changing heat-up of the parts with varying laser powers, the load temperature of the flash exposure heat source was adapted by the same percentage as the laser power changes.

Local heat source

Below, the procedure to determine the temperature behavior in the sub-models is described.

7

Governing equations. Within the sub-model regions, a moving heat source model based on the approach proposed by Goldak et al. [15] was applied. It considers a heat flux distribution q, representing the heat input into the considered material as a result of the interaction with the laser beam, and is calculated by

$$q(\xi, y, z, t) = \frac{6\sqrt{3} \cdot P \cdot \eta}{a \cdot b \cdot c \cdot \sqrt[3]{\pi}} \exp\left(-\frac{3\xi^2}{a^2} - \frac{3y^2}{b^2} - \frac{3z^2}{c^2}\right), \tag{1}$$

with

$$\xi = x + v \cdot (\tau - t). \tag{2}$$

The parameters a, b, and c describe the geometrical dimensions of the heat source, while ξ, y, and z represent the coordinates of a moving coordinate system. The origin of the latter is in the center of the heat source and moves with the laser beam scan speed v. The parameter P describes the laser power, η the efficiency, t the process time, and τ describes a lag factor. The latter is needed to define the heat source position at $t = 0$. The mentioned parameters are depicted in Figure 5.
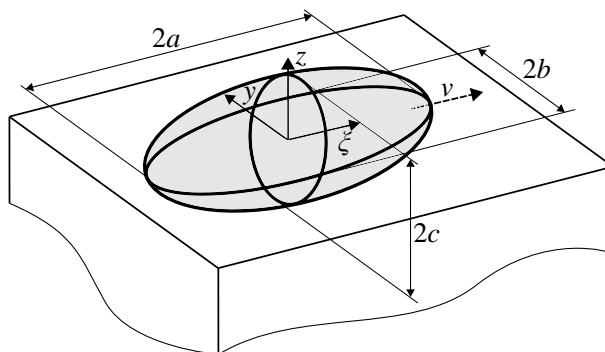

Figure 5: Dimensions and parameters of the moving heat source with the moving coordinate system axes ξ, y, and z, the heat source calibration parameters a, b, and c, and the laser beam scan speed v (adapted from Goldak et al. [15])

If not stated otherwise, the time steps in all moving heat source simulations were calculated as follows [16, 17]:

$$\Delta t < \frac{4\sigma}{3v}, \tag{3}$$

whereby σ represents the laser beam radius.

Heat source calibration. To determine the simulative melt pool dimensions for the local heat source calibration, a spatially reduced simulation domain was created with the global dimensions of $3 \times 2 \times 1 \, \text{mm}^3$ (see Figure 6). In this domain, the topmost $40 \, \mu\text{m}$ were assigned IN718 powder properties, while the lower remaining elements received the IN718 bulk material properties. This was in agreement with the experimental setup. The elements with powder properties were

assigned bulk material characteristics as soon as the heat source ellipsoid captured them. The simulated heat source was moving along the center region elements of the domain (melt pool elements), which were chosen to be 0.01 mm [7] and propagated 190 μm along the negative z-direction. The remaining elements in the powder layer (powder elements) and in the bulk (plate elements) were increased to 0.1 mm and 0.2 mm, respectively, with an element growth rate of 1.3. The thermal boundary conditions were set to be 353.15 K.

For the calibration process, the parameters a and b were chosen according to the laser beam focus point diameter, and c and η were iteratively adapted to strive for a match between the simulative and experimental melt pool widths and depths in the cross-section. For the latter two parameters, the heat source was calibrated separately for the highest and lowest laser powers, and validated for the middle power by linearly interpolating the two calibration parameters. This procedure was proposed by Shahabad et al. [18] and allows for a consideration of varying welding schemes, such as a transition from heat conduction towards keyhole welding.
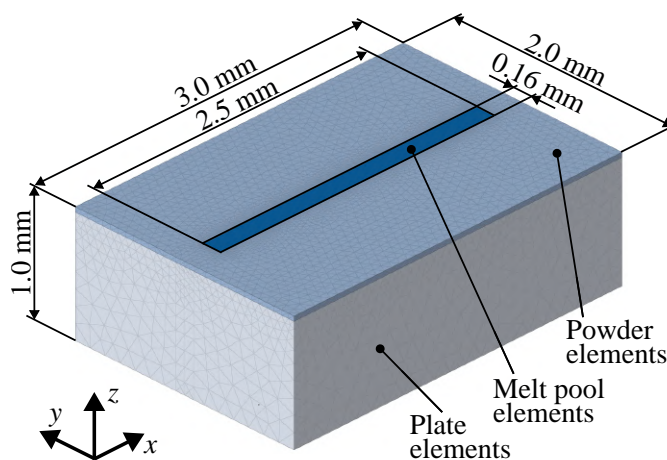

Figure 6: Dimensions of the moving heat source calibration and validation simulation domain with the building direction z

Sub-model simulation. The identified heat source values were then applied to the sub-model cuboids, which had the global dimensions of $0.6 \times 0.6 \times 1.0\,\text{mm}^3$. They were meshed with an element size of 0.02 mm. The corresponding elements were initially assigned the IN718 powder properties, which were changed to the bulk characteristics as in the single weld line simulations. The process parameters mentioned in Subsection 2.1.2 were utilized, and new layers were applied by the element birth and death approach [14]. After each layer, the bidirectional scan pattern was rotated by an angle of 67° as in the experiments. An increased cooling time was considered when the heat source reached the edge of the sub-model based on the current geometry cross-section to account for the laser beam return time in the experiments due to a stripe width greater than the sub-model size. The thermal boundary conditions of the sub-models were applied based on the global thermal simulations at various heights. The latter corresponded to the experimental microstructure evaluation locations 1 to 3 on the center line from the experiments (see Figure 3).

2.3.3 Nucleation modeling

The identified thermal values served as an input to a nucleation model. As highlighted by Panzer et al. [7], physics-based nucleation models on the basis of the heterogeneous nucleation theory allow for a first-time-right predictability of nucleation phenomena. Therefore, this model type was investigated further concerning process parameter variations and geometrical influences.

Model basis

Current physics-based nucleation models consider the calculation of the nucleation rate J, which is determined by

$$J = K \cdot \exp\left(-\frac{\Delta G^*}{k_{\mathrm{B}} \cdot T}\right) , \tag{4}$$

with ΔG^* representing the energy barrier at the critical nucleation radius, k_{B} the Boltzmann constant, and T the temperature. The kinetic pre-factor K is determined as follows:

$$K = \frac{2\sqrt{\gamma} \cdot f \cdot \lambda \cdot \rho_{\mathrm{l}}}{\sqrt{k_{\mathrm{B}} \cdot T \cdot \rho_{\mathrm{s}}}} \cdot \exp\left(-\frac{\Delta U}{k_{\mathrm{B}} \cdot T}\right) . \tag{5}$$

There, γ is the specific surface energy, f is the frequency factor, λ represents the mean free path of the particles in the liquid, and ρ_{l} and ρ_{s} are the number densities of the liquid and the solid, respectively, which describe the number of atoms per unit volume. ΔU represents the energy of desolvation. The energy barrier for the heterogeneous nucleation model is determined by

$$\Delta G^* = \frac{16\pi \cdot \gamma^3 \cdot T_{\mathrm{l}}^2}{3 \cdot \Delta h_{\mathrm{m}}^2 \cdot \Delta T^2 \cdot \rho_{\mathrm{s}}^2} \cdot S(\theta) , \tag{6}$$

with the liquidus temperature T_{l}, the molar enthalpy of melting Δh_{m}, and the undercooling ΔT. The shape factor $S(\theta)$ is calculated by

$$S(\theta) = (2 + \cos\theta)(1 - \cos\theta)^2/4 , \tag{7}$$

where θ represents the wetting angle, describing the spherical cap shape of a nucleus.

Conventional undercooling modeling

As it can be seen from the Equations 4 to 6, the nucleation rate is solely calculated by material parameters except for the absolute temperature T and the undercooling ΔT. While the temperature T is clearly defined by the temperature field of thermal simulations, the undercooling ΔT is composed of five components [19], from which mostly one term, the thermal undercooling, is utilized in PBF-LB/M microstructure simulations [20] due to its simplicity. The thermal undercooling is calculated by

$$\Delta T = T_{\mathrm{l}} - T . \tag{8}$$

However, the undercooling and the resulting nucleation and microstructure are strongly dependent on the temperature gradient and the solidification rate [8, 19, 21], highlighting the need

10

for an alternative undercooling modeling.

Alternative undercooling modeling

An approach for the calculation of the undercooling considering the temperature gradient G and the solidification rate R was formulated by Burden and Hunt [22] and proposed for PBF-LB/M by He and Webler [23] according to

$$\Delta T = \frac{GD_{\mathrm{l}}}{R} + m_{\mathrm{l}}c_0 \left(1 - \frac{1}{1 + (k-1)\Omega} \right) + \frac{\Gamma}{R} \; . \tag{9}$$

Here, D_{l} is the thermal diffusivity coefficient, m_{l} represents the slope of the liquidus line, c_0 is the initial solute concentration, k is the distribution coefficient, and Γ is the Gibbs-Thomson coefficient. The supersaturation Ω is calculated by

$$\Omega = \sqrt{\pi \cdot Pe} \cdot \exp\left(Pe \right) \cdot \mathrm{erfc}(\sqrt{Pe}) \; , \tag{10}$$

with the Peclet number Pe. The solidification rate R was calculated by tracking the velocity of the solidification front characterized by the solidus temperature T_{s} at the melt pool.

Numerical realization

For the determination of actual nucleation sites in the sub-model domain, a sub-mesh with a cell size of $1\,\mu\mathrm{m}$ was generated. Whether a cell was assigned a nucleus of critical size was determined by applying a Poisson seeding algorithm [24]. For this, the probability with which a nucleus is created is calculated by

$$P_{\mathrm{prob}} = 1 - \exp(-J \cdot V \cdot \Delta t) \; , \tag{11}$$

where V represents the volume of a sub-mesh cell size volume. To account for the probabilistic nucleation process [25], a field with random values P_i between 0 and 1 for each cell i was generated and compared to P_{prob}. A nucleation event was assumed to happen if

$$P_{\mathrm{prob}} > P_i \tag{12}$$

was fulfilled.

2.3.4 Material parameters

In the following, the utilized values for the material parameters for the thermal and the nucleation simulations are given.

Thermal simulation

The temperature-dependent material properties for IN718 and steel 1.1730 for the global simulations were taken from Seidel [26]. The IN718 values for the local simulations (thermal conductivity, specific heat capacity, and density) were extracted from Seidel [26] and Mills [27] and are visualized in Figure 7. The values of the thermal conductivity of the powder at $1448.15\,\mathrm{K}$ were increased to enhance the numerical stability of the moving heat source simulations.
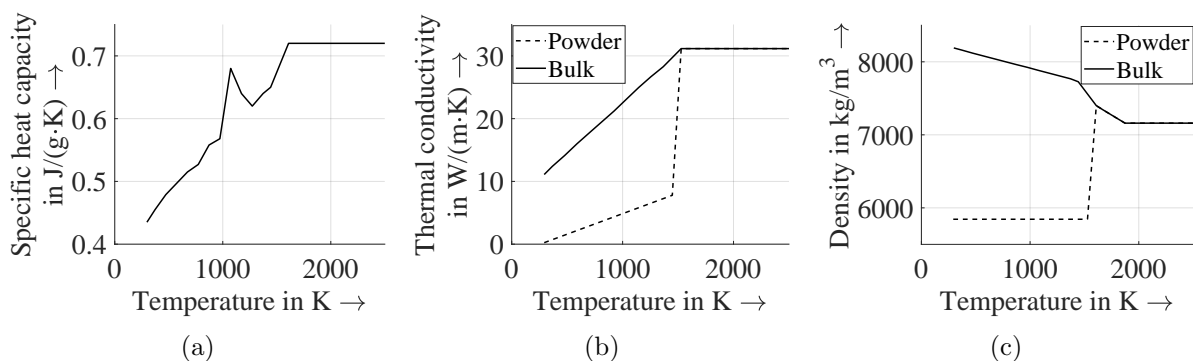
Figure 7: Bulk and powder material properties of IN718 for the local heat simulations (based on Seidel [26] and Mills [27]); (a) specific heat capacity (for powder and bulk), (b) thermal conductivity, (c) density

Nucleation simulation

Nucleation phenomena are especially relevant in the mushy zone, with its boundaries defined by the solidus and the liquidus temperature. Due to this bounded parameter space, the corresponding material values for the nucleation model were assumed to be constant and were derived as mean values within the mushy zone. The corresponding values needed to evaluate the nucleation behavior during PBF-LB/M, which were directly extracted from the literature, are given in Table 2.

Table 2: Material constants for the heterogeneous nucleation model for IN718; (*) adopted value for Inconel 740, as data for IN718 was not available

Material constant	Value	Reference
Boltzmann constant k_{B} in J/K	$1.38 \cdot 10^{-23}$	[28]
Frequency factor f in s^{-1}	$2.00 \cdot 10^{13}$	[29]
Energy of desolvation ΔU in kcal/mol	6.00	[29]
Solidus temperature T_{s} in K	1533.15	[9]
Liquidus temperature T_{l} in K	1613.15	[9]
Wetting angle θ (*) in °	104.00	[30]
Thermal diffusivity coefficient D_{l} in m^2/s	$5.60 \cdot 10^{-6}$	[27]
Slope of liquidus line m_{l} in K/m.%	-10.50	[31]
Initial solute concentration c_0 in m.%	5.00	[31]
Distribution coefficient k	0.58	[32]
Gibbs-Thomson coefficient Γ in K·m	$3.65 \cdot 10^{-7}$	[31]

The remaining values were calculated in the course of this study by weighting and averaging the parameter values of the individual elements according to the chemical composition of the utilized IN718 material [7]. The resulting values are given in Table 3.

12

Table 3: Self-calculated material constants for the heterogeneous nucleation model for IN718

Material constant	Value	Reference
Specific surface energy γ in J/m^2	0.267	[29, 33]
Mean free path λ in nm	15.690	[34, 35]
Number density (solid) $\rho_{\rm s}$ in cm^{-3}	$0.854 \cdot 10^{23}$	[36, 37]
Number density (liquid) $\rho_{\rm l}$ in cm^{-3}	$0.750 \cdot 10^{23}$	[36, 37]
Molar enthalpy of melting $\Delta h_{\rm m}$ in kJ/mol	18.243	[36]

2.3.5 Evaluation

In the following, the simulation evaluation procedure is described.

Thermal analysis

The global thermal simulation results of the specimens 1 and 2 were evaluated along the building direction at the center axis in the active layers after the cool-down. The values were compared to the results of the OT monitoring results and the surface annealing colors. The melt pool widths and depths of the local thermal simulations were evaluated in accordance with the experimental procedure, which is illustrated in Figure 2.

Nucleation and microstructure analysis

The local nucleation locations in the x-z-plane at individual melt pools in the multi-layer simulations were analyzed. The nucleation locations were compared to experimental grain structures on the same scale.

The global nucleation behavior was investigated by counting the number of nuclei in the x-z-plane in the center of the sub-model for the various laser powers and evaluation locations. The resulting calculated nucleation density was then compared to the grain density of the experiments at identical boundary conditions.

The predicted temperature gradients and solidification rates for a representative melt pool in the multi-layer simulation for the specimen 2 with the lowest and highest laser powers at the evaluation locations 1 and 3 were extracted. Afterwards, a qualitative grain type classification based on the thermal values was conducted. By this, it was intended to show that changes in the grain morphology with a changing thermal behavior during PBF-LB/M can be predicted without an actual simulation of the grain growth process.

3 RESULTS AND DISCUSSION

The experimental and simulative results as well as their comparisons are described and discussed below.

3.1 Thermal analysis

First, the heat source calibrations for the global and the local thermal simulations are evaluated. Also, their predictive capabilities in comparison with the experimental observations are presented.

3.1.1 Global heat source

The mesh convergence study and the thermal behavior are evaluated, starting with the global heat source.

Mesh convergence study

The results of the global mesh convergence study are shown in Figure 8 at build heights of 8 mm, 16 mm, and 24 mm for the specimen 2. It can be seen that with a decreasing element size, the temperature changes decreased, while the computation time strongly increased. At a build height of 8 mm, the temperature only changed by approximately 0.66 % from 708.52 °C to 713.23 °C when decreasing the element size from 1.0 mm to 0.5 mm. A similar behavior was observed for the other measurement heights. At the same time, the computation time increased by a factor of 10 from 1454.55 s to 14609.60 s. As the best compromise between numerical accuracy and computational effort, an element size of 1.0 mm was chosen for the remaining global thermal simulations.
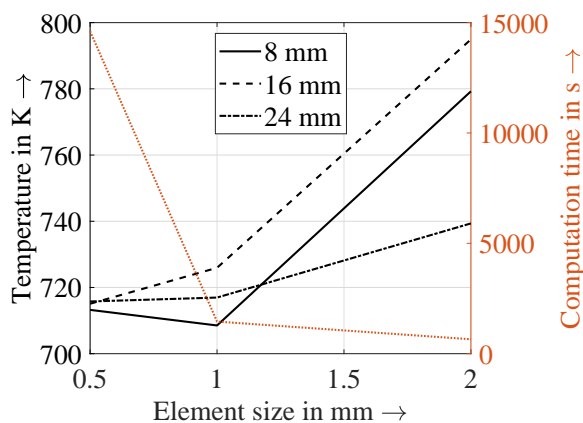

Figure 8: Mesh convergence results, evaluated at different build heights, and computation times for the specimen 2

Thermal behavior

Based on the global heat source calibration approach for the specimen 1, a cooling time of 60 s after each flash exposure was determined at which a temperature increase from the build plate temperature of 353.15 K towards the process temperature of 473.15 K along the building direction was realized. This situation is also visualized in Figure 9a for the high laser power, where the process temperature was reached at the top of the specimen. Applying the calibrated cooling time to the specimen 2, the temperature within the sample increased to a maximum temperature of approximately 900.15 K (see Figure 9b).

Comparing the global thermal behavior along the build height in Figure 9 with the annealing colors on the part surfaces after the actual building process in Figure 10, a similar behavior can be seen. While the specimen 1 did not exhibit any discoloration with an increasing build height (see Figure 10a), the specimen 2 showed a fluent color gradient at higher positions, which stagnated after reaching approximately two thirds of the total build height of the part (see
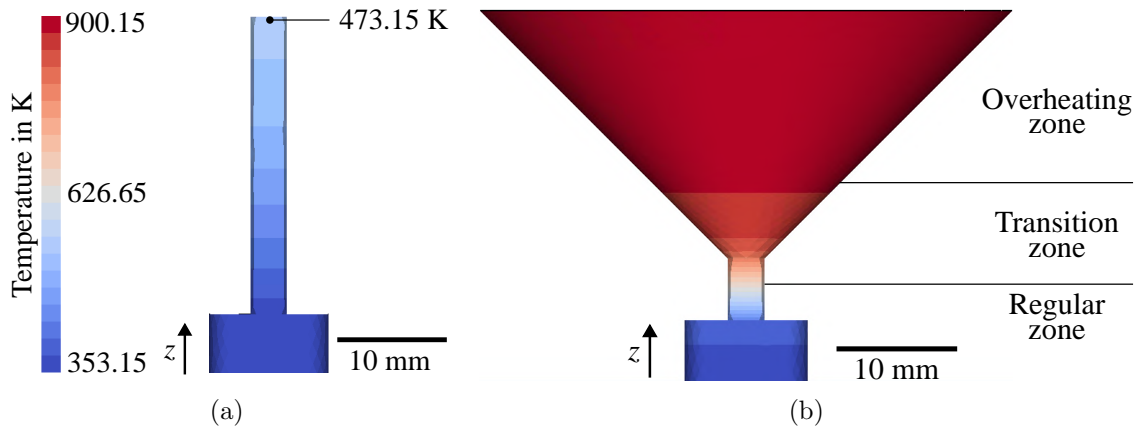
Figure 9: Geometrically induced overheating behavior in the simulation for the high laser power using the calibrated cooling time of 60 s with the building direction z; (a) specimen 1, (b) specimen 2

Figure 10b). The stagnating behavior is in accordance with the simulation results.
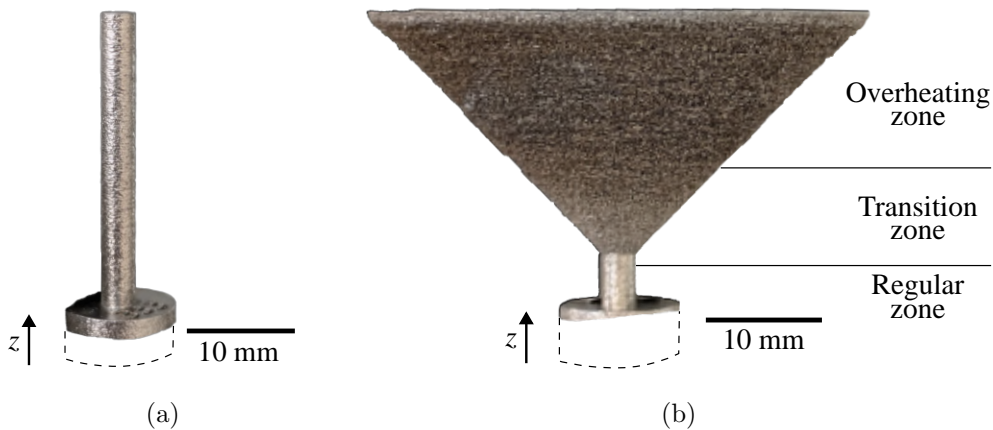

Figure 10: Geometrically induced overheating behavior in the experiments for the high laser power with the building direction z; (a) specimen 1, (b) specimen 2; the dashed lines illustrate the geometry before the cut-off process.

An analysis of the area-normalized integral OT data confirmed the observed characteristics of an increasing temperature field, followed by a stagnation, with an increasing build height for the specimen 2. The experimentally observed results, along with the corresponding simulation results, are depicted in Figure 11. Experimental outliers at the build heights 0 mm, 5 mm, and 30 mm can be seen, which were due to double exposures at the respective first or up-skin layers. Based on a comparison of the experimental and the simulative results, it can be observed that the geometry-related heat accumulations as well as the increased temperatures with the higher laser powers can be well predicted at increased build heights with the proposed overheating approach. However, the process parameter influence at low build heights was not accurately

represented. Nevertheless, the general trends showed that a single calibration value can be utilized for the representation of global geometrically induced heat accumulations along with laser power variations in the presented part-scale simulations.
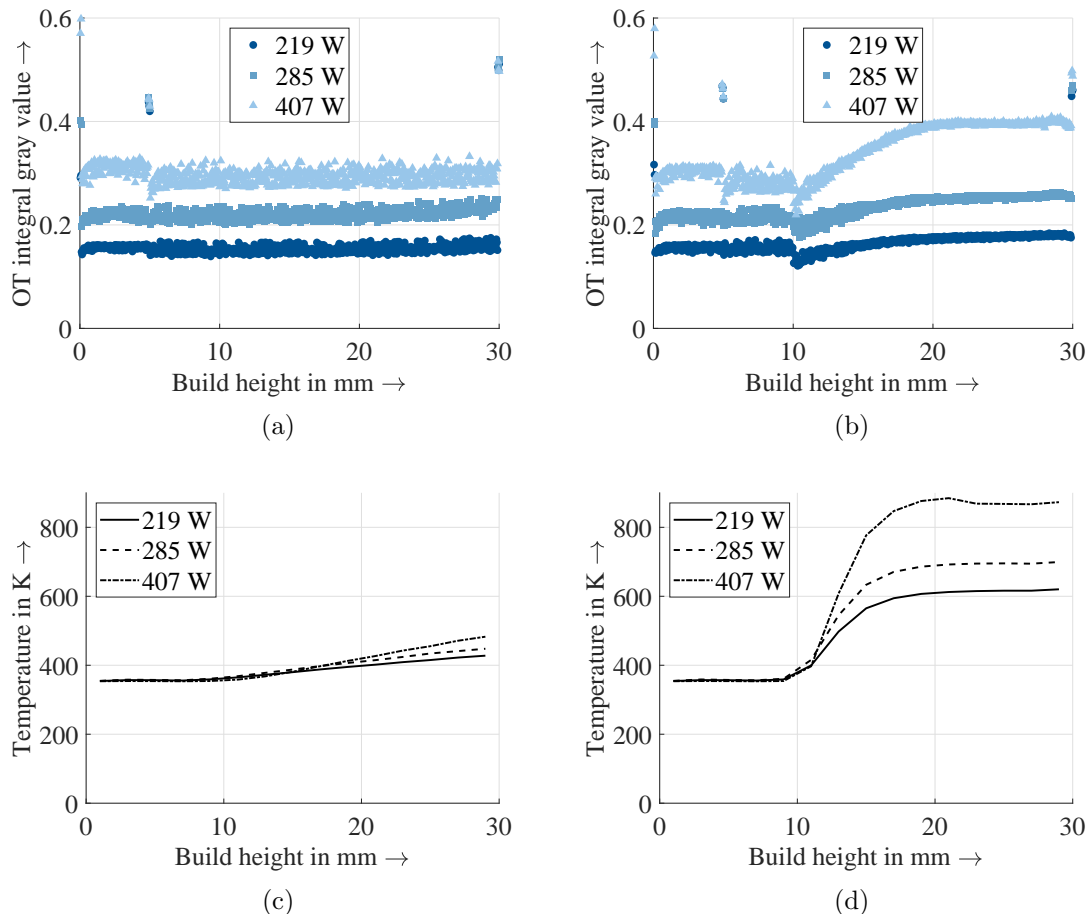

Figure 11: Thermal behavior with varying laser powers and geometries; (a) area-normalized integral OT gray values for the specimen 1, (b) area-normalized integral OT gray values for the specimen 2, (c) simulation results for the specimen 1, (d) simulation results for the specimen 2

The geometrically induced heat accumulation for the specimen 2 can be explained by the fact that the heat input increases with an increasing build height due to a growing cross-sectional area, into which a heat flow is generated through the laser beam. Also, the lower cylindrical part of the sample with a small diameter of 3 mm does not allow for a sufficient heat conduction into the build plate. For the specimen 1, the area of the cross-section remains constant, by which it becomes obvious that the heat input and the conduction are in balance. This results in a lower temperature growth along the build height. These observations of a geometrically induced heat accumulation are in accordance with results from the literature for various materials such as IN718 [38], Ti-6Al-4V [39, 40], and stainless steel 316L [41].

16

3.1.2 Local heat source

For the moving heat source, the time step chosen in the course of this study was $\Delta t = 35.42 \cdot 10^{-6}$ s, which was in accordance with Inequality 3. At the same time, the chosen time step size corresponded to a laser beam spot overlap of 80 % along the laser beam scan direction. The resulting calibration values for c and η were determined as listed in Table 4. The values for a and b were set to 0.045 mm according to the laser beam radius in the focus point.

Table 4: Heat source calibration values for the parameters c and η at different laser powers

Laser power	c	η
219 W	0.1000	0.5000
285 W	0.1491	0.5456
407 W	0.2400	0.6300

Based on these results, the simulatively determined melt pool dimensions were close to the mean values of the experimental dimensions and within their standard deviation for the three different laser power values, as illustrated in Figure 12. The fact, that also the melt pool dimensions for the medium laser power were well captured, highlights the validity of the applied calibration and validation approach. It can be observed that the melt pool width and depth increased with an increasing laser power due to an increased heat input. The increase of the melt pool depth was stronger, which can be attributed to a transition towards the keyhole melting mode, which has a higher impact on the melt pool depth compared to the width.
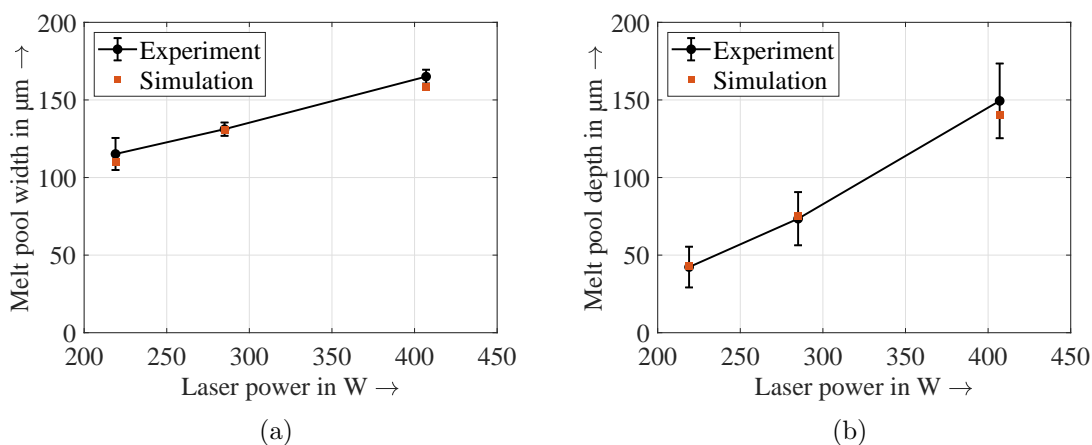

Figure 12: Comparison of the experimentally measured melt pool dimensions with the simulative results; (a) width, (b) depth

3.2 Nucleation and microstructure

In the following, the predictive capabilities of the adapted nucleation model with regard to local and global nucleation representations are analyzed and compared to experimental observations.

3.2.1 Local nucleation

The simulatively predicted nucleation locations were evaluated for the multi-layer sub-model. As exemplarily shown in Figure 13a for the medium laser power in the center of the specimen 2, the nucleation density at the sides of the melt pool borders was higher than in the center of the borders. Even though the complete melt pool was considered in the nucleation simulations, no nuclei were predicted in the bulk of the melt pool. These aspects were in accordance with the observations in the micrograph, showing the corresponding location in the experimentally built sample (see Figure 13b). Epitaxially grown grains migrating over multiple layer heights through the melt pool center can be seen, indicating no nucleation at this position. At the sides of the melt pool borders, newly formed grains were observed, which were initiated due to nuclei forming in these locations.
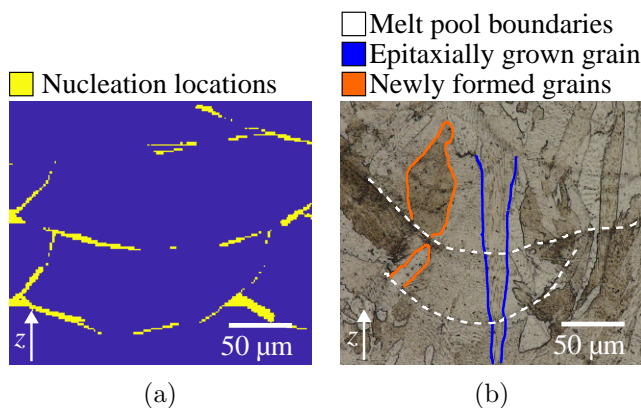

Figure 13: Local nucleation locations and resulting microstructures for the specimen 2 with the medium laser power in the center of the sample with the building direction z; (a) simulation, (b) experiment

Utilizing the conventional undercooling approach (see Equation 8), a continuous nucleation layer along the melt pool border was determined (not shown), as it only considers the current temperature in a respective point. The predicted nucleation behavior was, therefore, not in agreement with the microscopic evaluations. Hence, the correction of the nucleation locations by means of the adapted undercooling model based on Equation 9 was due to the consideration of the temperature gradient and the solidification rate.

Based on the alternative model and by considering the calculation of the nucleation rate, a stronger decrease of the thermal gradient compared to that of the solidification rate needs to be present at the sides of the melt pool borders, while the opposite is the case for the melt pool center. This can be explained by the fact that due to the overlap of two consecutive and parallel melt tracks in one layer, the melt pool sides of the successive track experience an increased temperature compared to the bottom part. This reduces the temperature gradient to a higher extent than the solidification rate. These analyses emphasize the necessity of taking the two thermal parameters into account when modeling nucleation phenomena.

3.2.2 Global nucleation

Below, the results of the global nucleation based on the simulations and the experiments are given and discussed.

Grain density and homogeneity

As depicted in Figure 14a, the simulation results for the specimens 1 and 2 showed a decreasing nucleation density with an increasing laser power. The starting point for the nucleation density was identical at the respective laser powers, which was to be expected as in this area the geometry shapes did not differ from each other.

While the nucleation density over the build height per laser power only decreased slightly between 3.5 % and 12.1 % for the specimen 1, a stronger reduction between 14.3 % and 50.3 % of the nucleation density for the specimen 2 was observed. This resulted in a less homogeneous microstructure in the latter sample. In both cases, the intensity of the decline along the build height correlated with the laser power, where an increase of this process parameter resulted in a respective nucleation reduction. These behaviors of a decreasing nucleation density with increasing laser powers and build heights can be attributed to a stronger decrease in the solidification rate compared to the thermal gradient, leading to a reduced nucleation rate.

It was also observed that for both specimen types a stagnation of the nucleation density from the evaluation location 2 to location 3 occurred. There, the strongest nucleation density decrease was determined to be 1.6 % for the specimen 1 and 7.5 % for the specimen 2. This was in agreement with the experimental observations considering the OT values and the annealing colors, and with the simulatively determined temperature values along the build height. All showed a similar stagnating behavior, which suggested a balance between the heat input and the conduction.

A behavior comparable to the simulations was observed in the microstructural investigations of the experiments, visualized in Figure 14b. The grain density at the first evaluation location overlapped for the two geometries at the corresponding laser powers. A decreasing grain density was observed with increasing laser powers. Also, the microstructural parameter remained mostly constant over the build height for the specimen 1, suggesting a homogeneous microstructure within the part, while a noticeable decline in the grain density was seen for the second sample. Contrary to the simulation results and the thermal experimental observations, no stagnation from the evaluation locations 2 to 3 was observed. This may be attributable to measuring inaccuracies of the applied grain analysis method, which is mainly based on contrast differences.

These findings are in agreement with observations in the literature for various materials. Coarser dendritic structures due to geometrically induced [38] or preheating-induced [42] heat accumulations were found for IN718. Those microstructural changes were found to be attributable to the varying thermal behavior such as the cooling rate [39, 40] with strong influences on the mechanical properties, such as the tensile strength [40] or the hardness [43].

Grain morphology

Utilizing a graphical representation for the temperature gradient and the solidification rate in Figure 15 [44], it was confirmed that, with an increasing build height, the microstructure tended to become coarser. This was due to a reduction of the temperature gradient and the solidification rate, and, therefore, of the cooling rate $G \times R$, which determines the grain size.
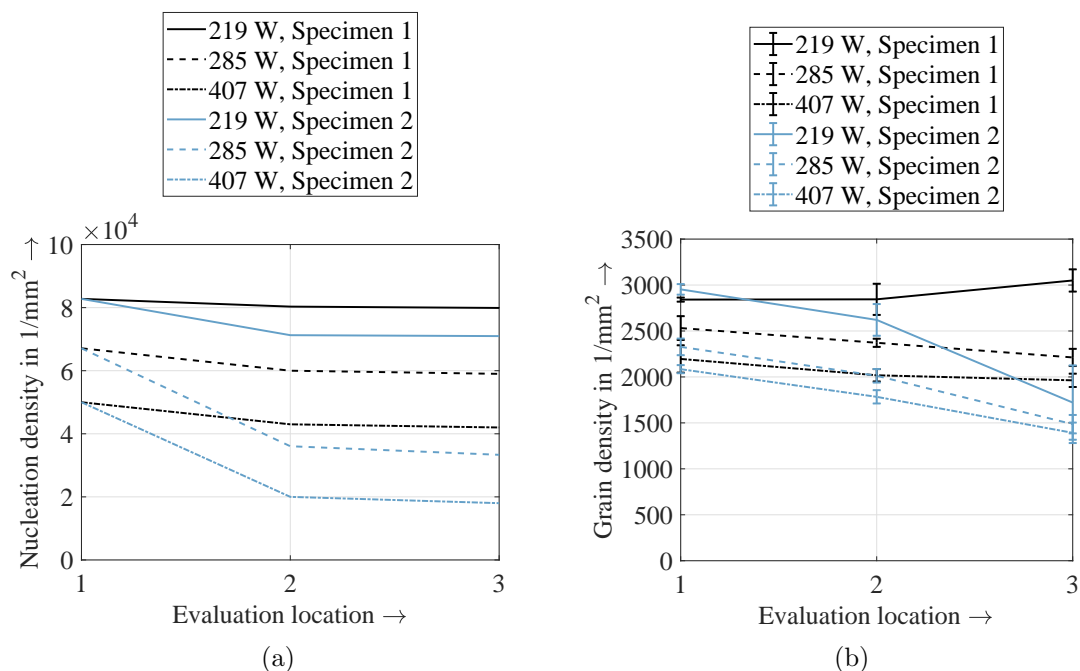
Figure 14: Global nucleation behavior and microstructure homogeneity; (a) simulation, (b) experiment

Additionally, the graph allows for a qualitative characterization of the grain morphology and its changes with varying process parameters and geometrically induced effects. When considering the mean values of the thermal results along one melt track in the multi-layer simulations, the microstructure tended to transform from a cellular to a columnar grain structure with an increasing laser power. This can be attributed to the fact that, with an increasing laser power, G increases and R decreases. By this, the solidification mode G/R increases, leading to a crystallographic lamellar grain structure, tending towards a single-crystal-like microstructure [21].

This qualitative observation was also in agreement with results from the literature. There, the solidification rate and the temperature gradient were utilized to qualitatively evaluate grain sizes and morphologies during PBF-LB/M [45], powder bed fusion of metals using an electron beam [46], and directed energy deposition of metals using a laser beam [47].

These observations match experimental studies, in which a strong epitaxial growth of columnar dendrites with an increasing volumetric energy density (VED) was observed [48, 49]. An increased grain alignment towards the <001> orientation along with an increased aspect ratio and grain diameter with an increasing VED in general [50] and specifically with an increasing laser power [51] was noticed. This was explained by the reduced cooling rate with an increasing VED, resulting in larger grains with a stronger texture [52].
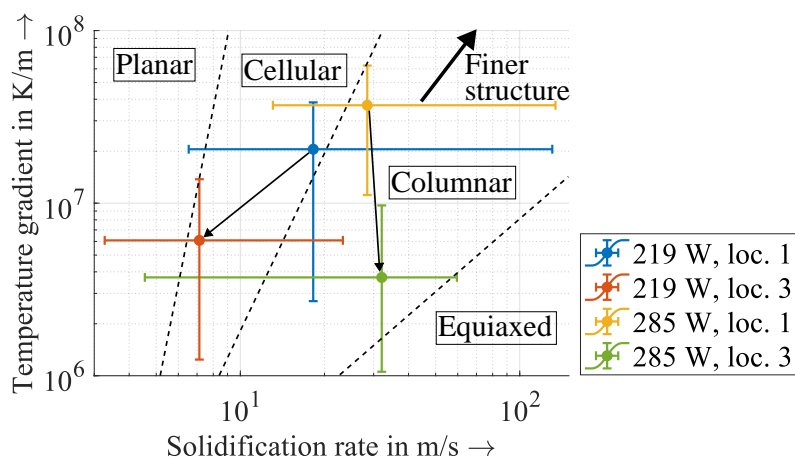
Figure 15: Qualitative grain morphology characterization and transition depending on the temperature gradient and the solidification rate for the specimen 2 at the medium laser power of 285 W

3.3 Critical discussion

The microstructural comparison between the simulative and the experimental results requires a compliance with the nucleation and grain behavior. For this study, the trends of both parameters are comparable to each other, as it can be assumed that every grain initiated from a nucleus. An extraction of information about absolute grain density values from the simulations should be seen skeptically and might need further adaptions.

Also, it needs to be considered that an interaction between cell capture events from growing grains, known as epitaxial nucleation [53], and nucleation events providing newly formed grains takes place in the mushy zone along the melt pool [54]. Therefore, the applicability of the alternative undercooling modeling approach for models considering grain growth, such as CA, should be investigated separately.

4 CONCLUSIONS AND OUTLOOK

Finally, the conclusions from this study are drawn, and an outlook concerning further investigations is given.

4.1 Conclusions

A multi-scale PBF-LB/M modeling approach was proposed, allowing for the identification of geometrically induced heat accumulations (macro-scale), the quantification of the influence of process parameter adaptions on the thermal behavior (meso-scale), and the prediction of nucleation locations (micro-scale). For the latter, an alternative undercooling modeling approach was utilized to consider the thermal gradient and the solidification rate. The predictive capabilities of the proposed method were experimentally validated on two different geometries and three different laser power values for each, utilizing the material IN718. The key findings of this study can be summarized as follows:

- The cylindrically and conically designed samples allowed for a comparison of geometrically

induced heat accumulation effects on the thermal behavior and the resulting microstructure. An overlay with changing laser powers allowed for a further variation of the thermal behavior.

- The proposed multi-scale approach enabled the consideration of geometrical features and process parameter changes. The macro-scale simulation captured the heat accumulation behavior in accordance with the experimentally observed temperature increase based on OT evaluations and surface discoloration investigations. It also proved to be an appropriate means to provide boundary conditions for the subsequently conducted meso-scale simulation applying a moving heat source, whose results were incorporated into the micro-scale nucleation simulation.

- The undercooling model of the micro-scale simulation was extended by taking into account the thermal gradient and the solidification rate. With this, the geometry-related and process-parameter-induced thermal effects were considered.

- The simulation showed accurate results for the local as well as the global nucleation predictions, and was in accordance with experimentally conducted grain structure analyses without requiring any model calibrations. This stand-alone nucleation approach is, therefore, applicable to determine grain density and homogeneity changes for varying geometries and process parameters. Also, qualitative changes in the grain morphology can be derived.

4.2 Outlook

Further adaptions of the nucleation model in terms of precipitates regarding their chemical composition and their coherence can be seen as research subjects for the future. This might be especially relevant for precipitation-hardening materials as the utilized IN718.
Additionally, the applicability of the nucleation modeling approach to simulations considering the grain growth should be investigated. Since additional phenomena influencing the grain formation take place in the mushy zone during the solidification process, an unmodified transferability of the nucleation model needs to be validated.

Author contributions

Hannes Panzer: Conceptualization; Methodology; Software; Validation; Formal analysis; Investigation; Data curation; Writing – original draft; Visualization. **Weiyu Zhao**: Investigation. **Oezguer Boeckuen**: Investigation. **Dominik Rauner**: Software; Writing – review & editing. **Luca Reichert**: Investigation. **Michael F. Zaeh**: Resources; Writing – review & editing; Supervision; Project administration; Funding acquisition.

Conflicts of interest

The authors declare no conflicts of interest.

REFERENCES

[1] N. Chen and M. C. Frank, "Design for manufacturing: Geometric manufacturability evaluation for five-axis milling," *Journal of Manufacturing Science and Engineering*, vol. 143, no. 8, 2021.

[2] H. Panzer, J. Diller, F. Ehrenfels, J. Brandt, and M. F. Zäh, "Experimental investigation of process parameter variations on the microstructure and failure behavior of IN718 structures in PBF-LB/M," *Journal of Laser Applications*, vol. 36, no. 1, 2024.

[3] J. Koepf, D. Soldner, M. Ramsperger, J. Mergheim, M. Markl, and C. Körner, "Numerical microstructure prediction by a coupled finite element cellular automaton model for selective electron beam melting," *Computational Materials Science*, vol. 162, pp. 148–155, 2019.

[4] Q. Xie, X. Yan, S. Yin, X. Li, M. Liu, Y. Wang, and L. Zhuang, "An extended version of cellular automata model for powder bed fusion to unravel the dependence of microstructure on printing areas for Inconel 625," *Additive Manufacturing*, vol. 73, no. 103676, 2023.

[5] A. R. A. Dezfoli, W.-S. Hwang, W.-C. Huang, and T.-W. Tsai, "Determination and controlling of grain structure of metals after laser incidence: Theoretical approach," *Scientific Reports*, vol. 7, no. 41527, 2017.

[6] X. Li and W. Tan, "Numerical investigation of effects of nucleation mechanisms on grain structure in metal additive manufacturing," *Computational Materials Science*, vol. 153, pp. 159–169, 2018.

[7] H. Panzer, L. Buss, and M. F. Zaeh, "Enhancing the predictive capabilities of microstructure simulations of PBF-LB/M by an evaluation of nucleation theories," *Metallurgical and Materials Transactions A*, vol. 54, no. 4, pp. 1142–1158, 2023.

[8] M. S. Mohebbi and V. Ploshikhin, "Implementation of nucleation in cellular automaton simulation of microstructural evolution during additive manufacturing of al alloys," *Additive Manufacturing*, vol. 36, no. 101726, 2020.

[9] "Material product data sheet – 718 nickel alloy for additive manufacturing," tech. rep., Oerlikon Metco, 2024.

[10] C. A. Schneider, W. S. Rasband, and K. W. Eliceiri, "NIH image to ImageJ: 25 years of image analysis," *Nature Methods*, vol. 9, no. 7, pp. 671–675, 2012.

[11] F. A. Bayerlein, *Managing Form Deviation in Laser Beam Melting by Pre-Deformation*. PhD thesis, Technical University of Munich, 2020.

[12] D. Goetz, H. Panzer, D. Wolf, F. Bayerlein, J. Spachtholz, and M. F. Zaeh, "AscentAM: A software tool for the thermo-mechanical process simulation of form deviations and residual stresses in powder bed fusion of metals using a laser beam," *Modelling*, vol. 5, no. 3, pp. 841–860, 2024.

[13] G. Dhondt, "Calculix crunchix user's manual version 2.20," 2022.

[14] S. Afazov, W. A. Denmark, B. L. Toralles, A. Holloway, and A. Yaghi, "Distortion prediction and compensation in selective laser melting," *Additive Manufacturing*, vol. 17, pp. 15–22, 2017.

[15] J. Goldak, A. Chakravarti, and M. Bibby, "A new finite element model for welding heat sources," *Metallurgical Transactions B*, vol. 15, no. 2, pp. 299–305, 1984.

[16] E. J. Schwalbach, S. P. Donegan, M. G. Chapman, K. J. Chaput, and M. A. Groeber, "A discrete source model of powder bed fusion additive manufacturing thermal history," *Additive Manufacturing*, vol. 25, pp. 485–498, 2019.

[17] K. Teferra and D. J. Rowenhorst, "Optimizing the cellular automata finite element model for additive manufacturing to simulate large microstructures," *Acta Materialia*, vol. 213, no. 116930, 2021.

[18] S. I. Shahabad, Z. Zhang, A. Keshavarzkermani, U. Ali, Y. Mahmoodkhani, R. Esmaeilizadeh, A. Bonakdar, and E. Toyserkani, "Heat source model calibration for thermal analysis of laser powder-bed fusion," *The International Journal of Advanced Manufacturing Technology*, vol. 106, no. 7–8, pp. 3367–3379, 2020.

[19] D. M. Stefanescu and R. Ruxanda, "Fundamentals of solidification," pp. 71–92, 2004.

[20] C. Körner, M. Markl, and J. A. Koepf, "Modeling and simulation of microstructure evolution for additive manufacturing of metals: A critical review," *Metallurgical and Materials Transactions A*, vol. 51, no. 10, pp. 4970–4983, 2020.

[21] O. Gokcekaya, T. Ishimoto, S. Hibino, J. Yasutomi, T. Narushima, and T. Nakano, "Unique crystallographic texture formation in inconel 718 by laser powder bed fusion and its effect on mechanical anisotropy," *Acta Materialia*, vol. 212, no. 116876, 2021.

[22] M. Burden and J. Hunt, "Cellular and dendritic growth. II," *Journal of Crystal Growth*, vol. 22, no. 2, pp. 109–116, 1974.

[23] Y. He and B. Webler, "A solidification mode selection process map for laser powder bed fusion additive manufacturing of B-modified Ti6Al4V," *Additive Manufacturing*, vol. 59, no. 103086, 2022.

[24] R. Shi, S. Khairallah, T. W. Heo, M. Rolchigo, J. T. McKeown, and M. J. Matthews, "Integrated simulation framework for additively manufactured Ti-6Al-4V: Melt pool dynamics, microstructure, solid-state phase transformation, and microelastic response," *JOM*, vol. 71, no. 10, pp. 3640–3655, 2019.

[25] J. H. K. Tan, S. L. Sing, and W. Y. Yeong, "Microstructure modelling for metallic additive manufacturing: a review," *Virtual and Physical Prototyping*, vol. 15, no. 1, pp. 87–105, 2019.

[26] C. M. Seidel, *Finite-Elemente-Simulation des Aufbauprozesses beim Laserstrahlschmelzen (engl.: Finite Element Simulation of the Build-Up Process during Laser Beam Melting)*, vol. 351. utzverlag GmbH, 2016.

[27] K. C. Mills, *Recommended values of thermophysical properties for selected commercial alloys.* Woodhead Publishing, 2002.

[28] D. B. Newell and E. Tiesinga, "The international system of units (SI)," *NIST Special Publication*, vol. 330, pp. 1–138, 2019.

[29] I. V. Markov, *Crystal growth for beginners: fundamentals of nucleation, crystal growth and epitaxy.* Singapore: World scientific, 2016. pp. 77–181.

[30] N. Sobczak, R. Purgert, R. Asthana, J. Sobczak, M. Homa, R. Nowak, G. Bruzda, A. Siewiorek, and Z. Pirowski, "Wettability and reactivity of Y2O3 with liquid nickel and its alloys," *Ceramic Engineering and Science Proceedings*, pp. 307–321, 2015.

[31] P. Nie, O. Ojo, and Z. Li, "Numerical modeling of microstructure evolution during laser additive manufacturing of a nickel-based superalloy," *Acta Materialia*, vol. 77, pp. 85–95, 2014.

[32] N. Kropotin, Y. Fang, C. Yu, M. Seyring, K. Freiberg, S. Lippmann, T. Pinomaa, A. Laukkanen, N. Provatas, and P. K. Galenko, "Modelling of the solidifying microstructure of inconel 718: Quasi-binary approximation," *Modelling*, vol. 4, no. 3, pp. 323–335, 2023.

[33] D. A. Porter and K. E. Easterling, *Phase transformations in metals and alloys (revised reprint).* CRC press, 2009.

[34] D. Gall, "Electron mean free path in elemental metals," *Journal of Applied Physics*, vol. 119, no. 085101, 2016.

[35] S. Tanuma, C. Powell, and D. Penn, "Calculations of electron inelastic mean free paths. IX. data for 41 elemental solids over the 50 eV to 30 keV range," *Surface and interface analysis*, vol. 43, pp. 689–713, 2011.

[36] J. J. Valencia and P. N. Quested, *Thermophysical properties*, vol. 15, pp. 468–481. ASM, 2008.

[37] J. Meija, T. B. Coplen, M. Berglund, W. A. Brand, P. De Bièvre, M. Gröning, N. E. Holden, J. Irrgeher, R. D. Loss, T. Walczyk, *et al.*, "Atomic weights of the elements 2013 (IUPAC technical report)," *Pure and Applied Chemistry*, vol. 88, pp. 265–291, 2016.

[38] J. Zielinski, J. Theunissen, H. Kruse, S.-K. Rittinghaus, J. H. Schleifenbaum, D. Zhu, and M. Megahed, "Understanding inhomogeneous mechanical properties in PBF-LB/M manufactured parts due to inhomogeneous macro temperature profiles based on process-inherent preheating," *Journal of Manufacturing and Materials Processing*, vol. 7, no. 3, 2023.

[39] F. Nahr, M. Rasch, C. Burkhardt, J. Renner, B. Baumgärtner, T. Hausotte, C. Körner, P. Steinmann, J. Mergheim, M. Schmidt, and M. Markl, "Geometrical influence on material properties for Ti6Al4V parts in powder bed fusion," *Journal of Manufacturing and Materials Processing*, vol. 7, no. 3, 2023.

[40] J. Munk, E. Breitbarth, T. Siemer, N. Pirch, and C. Häfner, "Geometry effect on microstructure and mechanical properties in laser powder bed fusion of Ti-6Al-4V," *Metals*, vol. 12, no. 3, 2022.

[41] G. Mohr, N. Scheuschner, and K. Hilgenberg, "In situ heat accumulation by geometrical features obstructing heat flux and by reduced inter layer times in laser powder bed fusion of aisi 316l stainless steel," *Procedia CIRP*, vol. 94, pp. 155–160, 2020.

[42] H. T. Chowdhury, T. N. Palleda, N. Kakuta, and K. Kakehi, "Effects of preheating on thermal behavior in inconel 718 processed by additive manufacturing," *Thermo*, vol. 4, no. 1, pp. 48–64, 2024.

[43] Z. Y. Chua, S. K. Moon, L. Jiao, and I. H. Ahn, "Geometric influence of the laser-based powder bed fusion process in Ti6Al4V and AlSi10Mg," *The International Journal of Advanced Manufacturing Technology*, vol. 114, no. 9–10, pp. 3165–3176, 2021.

[44] S. Kou, "Welding metallurgy," *New Jersey, USA*, vol. 431, pp. 223–225, 2003.

[45] J. Yoshioka and M. Eshraghi, "Temporal evolution of temperature gradient and solidification rate in laser powder bed fusion additive manufacturing," *Heat and Mass Transfer*, vol. 59, no. 7, pp. 1155–1166, 2022.

[46] N. Raghavan, *Understanding Process-Structure Relationship For Site-Specific Microstructure Control in Electron Beam Powder Bed Additive Manufacturing Process Using Numerical Modeling.* PhD thesis, University of Tennessee, 2017.

[47] C. Hagenlocher, P. O'Toole, W. Xu, M. Brandt, M. Easton, and A. Molotnikov, "The effect of heat accumulation on the local grain structure in laser-directed energy deposition of aluminium," *Metals*, vol. 12, no. 10, 2022.

[48] Q. Jia and D. Gu, "Selective laser melting additive manufacturing of inconel 718 superalloy parts: Densification, microstructure and properties," *Journal of Alloys and Compounds*, vol. 585, pp. 713–721, 2014.

[49] K. Moussaoui, W. Rubio, M. Mousseigne, T. Sultan, and F. Rezai, "Effects of selective laser melting additive manufacturing parameters of inconel 718 on porosity, microstructure and mechanical properties," *Materials Science and Engineering: A*, vol. 735, pp. 182–190, 2018.

[50] V. Praveen Kumar and A. Vinoth Jebaraj, "Microscale investigations on additively manufactured inconel 718: influence of volumetric energy density on microstructure, texture evolution, defects control and residual stress," *Applied Physics A*, vol. 129, no. 5, 2023.

[51] S. Ghorbanpour, K. Deshmukh, S. Sahu, T. Riemslag, E. Reinton, E. Borisov, A. Popovich, V. Bertolo, Q. Jiang, M. T. Sanchez, M. Knezevic, and V. Popovich, "Additive manufacturing of functionally graded Inconel 718: Effect of heat treatment and building orientation on microstructure and fatigue behaviour," *Journal of Materials Processing Technology*, vol. 306, no. 117573, 2022.

[52] S. Pramod and D. Kesavan, "Melting modes of laser powder bed fusion (L-PBF) processed IN718 alloy: Prediction and experimental analysis," *Advances in Industrial and Manufacturing Engineering*, vol. 6, no. 100106, 2023.

[53] C. Herriott, X. Li, N. Kouraytem, V. Tari, W. Tan, B. Anglin, A. D. Rollett, and A. D. Spear, "A multi-scale, multi-physics modeling framework to predict spatial variation of properties in additive-manufactured metals," *Modelling and Simulation in Materials Science and Engineering*, vol. 27, no. 2, 2019.

[54] Y. Chen, Y. Wang, H. Li, Y. Lu, B. Han, and Q. Zhang, "Effects of process parameters on the microstructure of inconel 718 during powder bed fusion based on cellular automata approach," *Virtual and Physical Prototyping*, vol. 18, no. 1, 2023.